The dynamic flow behaviour of an oar blade in motion using a hydrodynamics-based shell-velocity-coupled model of a rowing stroke

A Sliasas* and **S Tullis**
Department of Mechanical Engineering, McMaster University, Hamilton, Ontario, Canada

The manuscript was received on 17 August 2009 and was accepted after revision for publication on 26 November 2009.

DOI: 10.1243/17543371JSET57

Abstract: The flow around a rowing oar blade during a stroke is highly complex owing to the proximity of the water surface and the rapidly changing blade flow incidence (here, greater than 180° in under 0.75 s). This flow is simulated using a computational fluid dynamics (CFD) model with a rotating subdomain for blade rotation coupled to a model of the shell velocity. Based on the shell velocity and a specified oar angular velocity, the CFD model calculates the highly unsteady three-dimensional flow, providing instantaneous drag, lift, and propulsive forces on the blade. The propulsive force drives the shell velocity model, which also accounts for the shell drag and the motion of the rowers relative to the shell. The dynamic blade–water interaction is depicted in six distinct flow regimes, characterized by the relative motion of the blade and the temporal influence of drag and lift. It is seen that the propulsive force generated by the blade is largely lift induced during the first half of the stroke. Dynamic stall behaviour of the blade characterizes the flow during the second half of the stroke, where drag increasingly influences the propulsive force. At the end of the stroke, the propulsive force is once again largely lift induced.

Keywords: rowing, blade, modelling, hydrodynamics, computational fluid dynamics, free-surface flow

1 INTRODUCTION

The hydrodynamics of a rowing oar blade in motion during a stroke are highly complex. Attempts to examine this flow quantitatively, through modelling or experiments, have had limited success owing to the combination of a strongly three-dimensional flow character, the proximity of the blade to the water surface, and the highly transient nature of the stroke. Analytical models of rowing stroke hydrodynamics generally only consider flow in one or two dimensions, which is insufficient for discerning the true flow behaviour. Experimental work has also been largely unsuccessful, because of the difficulty both in obtaining pertinent data from actual rowing conditions, and in replicating the complex rowing motion within a laboratory. It is this interacting motion of the rower, shell, oar, and water which provides the basis for the present study.

**Corresponding author: Department of Mechanical Engineering, McMaster University, 1280 Main St W., Hamilton, Ontario L8S 4L8, Canada.*
email: sliasaae@mcmaster.ca

1.1 The rowing stroke

The complete rowing stroke consists of two phases: the *drive* and the *recovery*. At the beginning of the drive (the *catch*), the propulsive portion of the stroke, the rower has their legs bent and arms outstretched while leaning towards the stern. The blade is planted in the water as the rower accelerates their body towards the bow, prying the shell ahead by extending the legs, leaning back, and drawing the arms into the chest in a sequential yet fluid motion. Throughout the stroke, the top edge of the blade remains buried slightly below the surface of the water. Viewed from a stationary perspective, the oar blade is locked in a pocket of water throughout the drive, acting as an axis for the shell to lever about. At the end of the drive (the *finish*), the oar is removed from the water and the rower approaches the stern, moving into position for the next stroke as the shell glides forwards. A

closer look at the blade with respect to the water during the drive indicates that the blade moves within the pocket, both parallel and lateral to the shell motion. The nature of this blade motion in the water is largely what determines shell propulsion.

1.2 Blade motion theory

As a starting point in understanding the nature of the flow about the blade, it is beneficial to look at its path traced through the water during the drive from a stationary frame of reference with respect to the accelerating shell. Kleshnev [**1**] was one of the first to observe that, when viewed from above, the centre of the blade chord line moves in a *figure-nine* pattern during the drive (Fig. 1).

The shell is moving from left to right, with the blade beginning at the bottom left corner at the catch. Through the stroke the blade moves simultaneously both parallel and lateral to the motion of the shell. The movement of the blade parallel to the motion of the shell is known as *slip*. Positive slip is defined as motion in the same direction as the shell velocity, whereas negative slip is opposite to the shell velocity. The lateral motion of the blade is due to the sweep of the oar; the blade moves away from the shell at the beginning of the drive, becoming orthogonal to the shell, and then moves back towards the shell near the end of the drive.

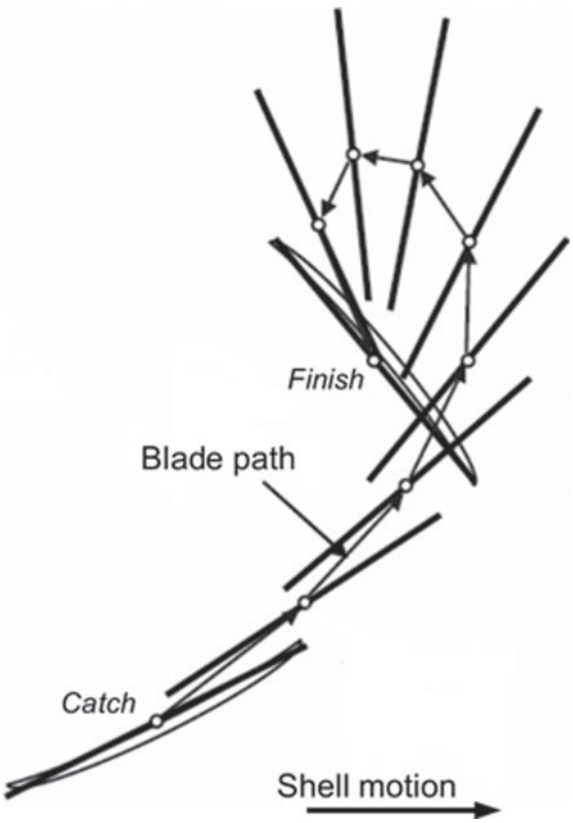

Fig. 1 From a stationary perspective, an overhead view of the approximate path of the centre of the blade chord line through the water during a stroke. The shell is moving from left to right. (Adapted with permission from Kleshnev [**1**])

Combining the linear velocity $\boldsymbol{v}_{\text{shell}}$ of the shell with the angular velocity $\boldsymbol{\omega}_{\text{oar}}$ of the oar, there is a relative flow velocity $\boldsymbol{v}_{\text{relative}}$ incident on the blade (Fig. 2). The nominal angle of attack on the blade, $\boldsymbol{\alpha}_{\text{nominal}}$, is the angle of incidence of on the midpoint of the blade $\boldsymbol{v}_{\text{relative}}$ chord line. Although the true angle of attack varies along the length of the chord because of the rotation of the oar, the use of $\boldsymbol{\alpha}_{\text{nominal}}$ is useful in defining a reference for the relative flow on the blade. Acting in line with this relative flow is a drag force $\boldsymbol{F}_{\text{drag}}$ on the blade, and acting perpendicularly is a lift force $\boldsymbol{F}_{\text{lift}}$. The net resultant force $\boldsymbol{F}_{\text{net,blade}}$ on the blade is the vector sum of the drag and lift forces.

Through the early portion of the drive, the relative flow approaches the blade tip with a very shallow nominal angle of attack (of approximately 0°). During the short time that the blade is in the water during the drive (less than 0.75 s), the flow sweeps an arc of approximately 190° across the surface, eventually becoming incident on the back (convex) surface. These highly transient characteristics combined with the constantly evolving water surface near the blade make understanding the dynamic three-dimensional flow behaviour quite difficult. It is in this regard where previous models have had shortcomings.

1.3 Previous rowing models

It should be noted that a rowing model can at best be employed as a predictor of relative results. Outcomes of elite-level 2000 m rowing races are often decided by only several metres (differences of 0.1 per cent over the course of an entire race). Influences external to the equipment (the rowers, weather conditions, etc.) certainly impact heavily on race outcomes. The relative speed advantage that can be obtained with an isolated change in equipment, however, with other factors held constant, can be measured using an appropriate model.

The majority of existing rowing models are analytical in nature, attempting to simulate the velocity of a shell by simplifying the forces involved. One such model was proposed by Millward [**2**] and is based on a force balance on the shell, where the force generated by the oar blade in the water is opposed by a drag force on the shell. It was assumed that the oar rotates about a stationary vertical axis located through the centre of the blade, which remains fixed in the water through the drive. The force applied at the oar handle, then, is fully transmitted to the water through the blade. This simplification is analogous to perfect efficiency in transferring power from the rower to the water, neglecting any hydrodynamic

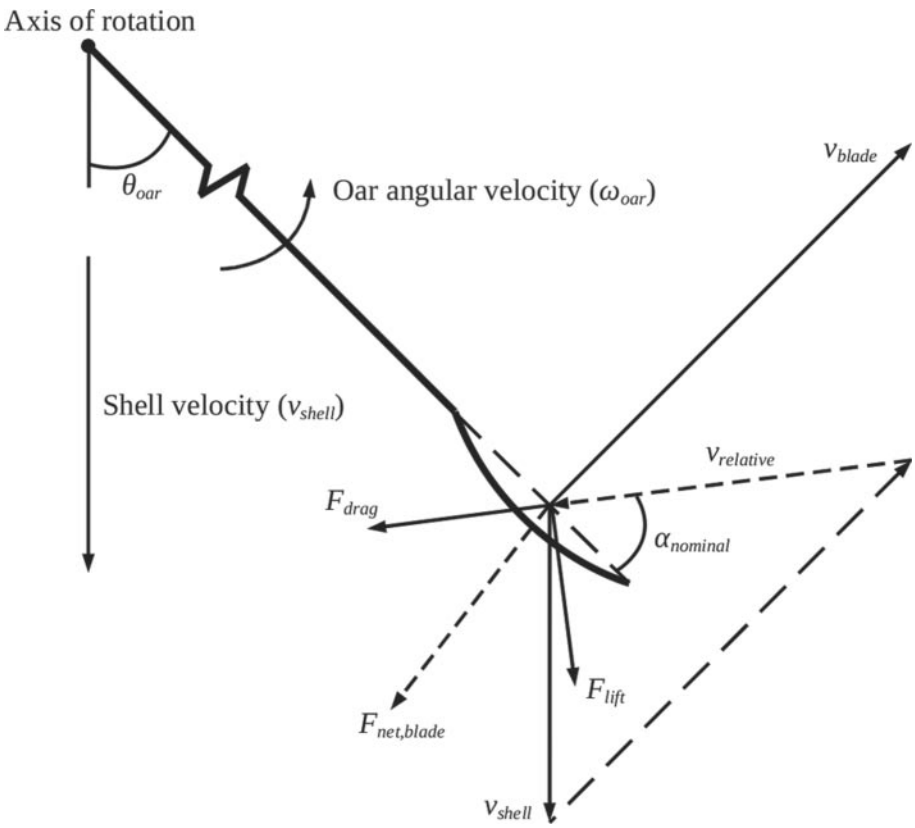

Fig. 2 Overhead view of a rotating rowing oar during a stroke. The shell is moving downwards and the oar is rotating counterclockwise, resulting in a relative flow on the blade. The net force on the blade, broken into drag and lift components, is indicated

characteristics of the blade. The rowers were also treated as stationary within the shell, neglecting the effect of their motion on the momentum of the shell. A model by Brearley *et al.* [**3**] was similar to the model by Millward, except that it accounted for the motion of the rowers within the shell. This model still contained the limiting behaviour of the blade acting as a fixed vertical axis in the water, however.

Pope [**4**] accounted for blade motion in his model, hypothesizing that only the component of the relative blade flow incident normal to its chord line was responsible for the generated blade force; i.e. he assumed that the blade only experiences drag as it moves through the water. The direction of the resultant blade force, then, always acts perpendicular to the blade chord line throughout the stroke. The magnitude of this blade force is proportional to the square of the relative blade velocity and was calculated, in the absence of more appropriate data, using drag coefficients for a surface-piercing flat plate. Wellicome [**5**] suggested that this resultant force was not always perpendicular to the blade surface during the stroke, owing to the presence of generated vortices trailing the blade. Nolte [**6**] further argued that the blade also generates lift, acting like a hydrofoil, particularly near the beginning of the drive. Models by Caplan and Gardner [**7**] and Atkinson [**8**] take into account both drag and lift forces on the blade throughout the stroke. These hydrodynamic forces were determined using available drag and lift coefficients for a stationary rowing blade [**9**]. A study by Macrossan [**10**], however, noted that drag and lift characteristics of a stationary rowing blade probably differ substantially from those for a blade in motion. Computational fluid dynamic (CFD) simulations carried out by Sliasas and Tullis [**11**] highlighted the highly unsteady behaviour of the blade–water interaction during the drive. They argued that the resultant force on a blade in motion is strongly dependent on developed three-dimensional flow conditions and therefore cannot be resolved using static flow techniques. As a result, their simulation showed that the drag and lift characteristics determined by Caplan and Gardner [**9**] for a stationary blade differ greatly from those for a blade in motion. A shortcoming of the simulation by Sliasas and Tullis [**11**] was that it required experimentally obtained input of both shell velocity and oar angular velocity. This restriction made the numerical model susceptible to any error in the coupled experimental data. In addition, data of this nature are limited, minimizing

the flexibility of the model to simulate only the available cases.

This paper begins with an outline of the development of a hydrodynamics-based model of the rowing stroke, simulating the resultant shell velocity based on the conditions of the stroke. A detailed hydrodynamic examination of the unsteady blade–water interaction during the drive ensues. Six distinct flow phases occurring during the drive are outlined, and their impact on the motion of the shell are discussed.

2 METHODS

To model the unsteady interaction of a blade in the water during the drive, a transient CFD simulation was created using the ANSYS CFX software package (ANSYS Inc., USA). The frame of reference is based on an accelerating shell, and the unsteady effects of the free-surface flow about the blade are fully simulated. By specifying the angular velocity of the oar, the shell velocity is calculated on the basis of the propulsive force generated by the blade in the water, an analytical treatment of the drag on the shell, and the momentum resulting from the motion of the rowers (the *crew*) with respect to the shell.

2.1 Model domain

The physical domain, modelling a full-scale blade in open water conditions, consists of a 10 m × 10 m × 2 m deep volume with a water depth of 1.5 m and a region of air above (Fig. 3). A cylindrical rotating domain of

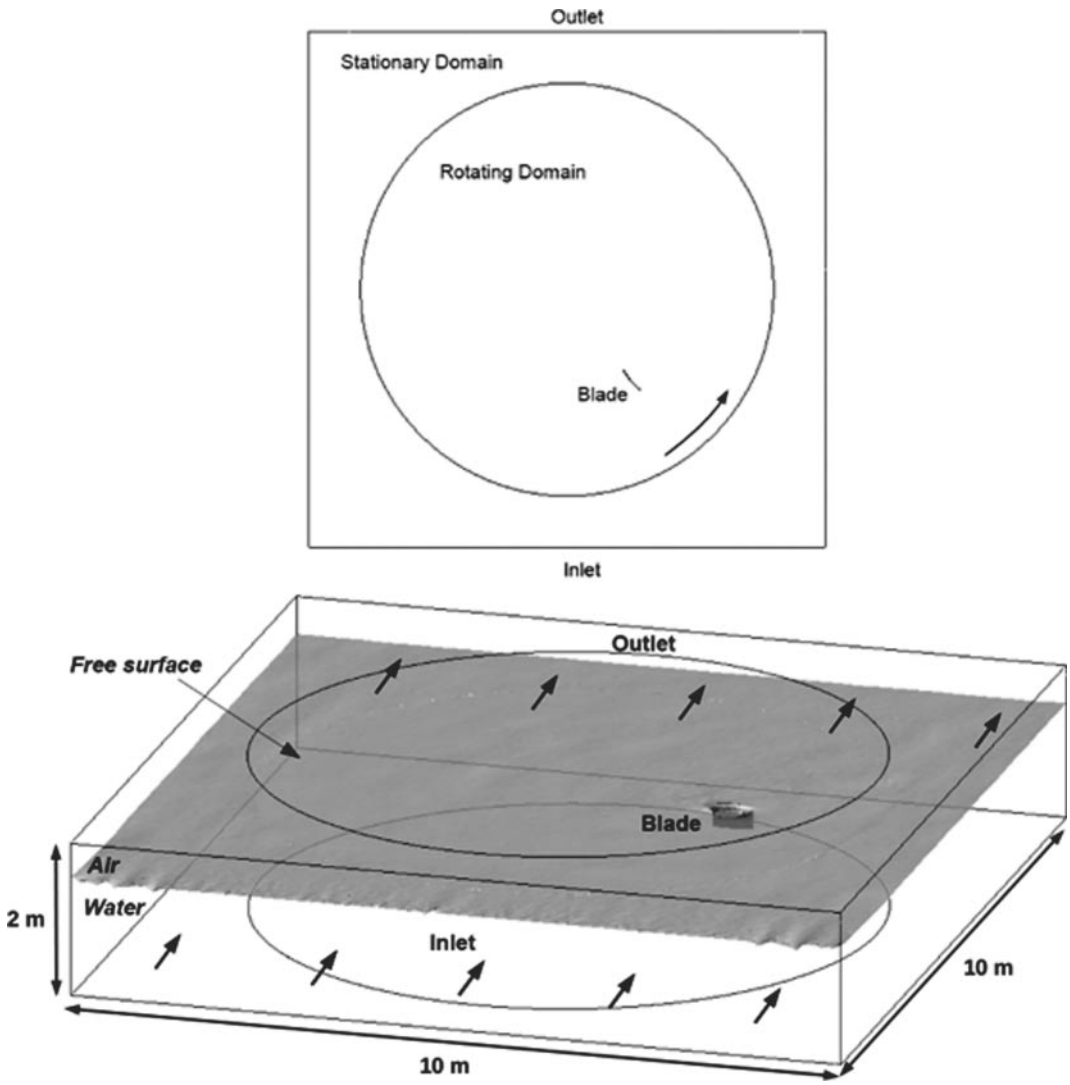

Fig. 3 Overhead and isometric views of the model domain. The inner cylindrical rotating domain, containing the blade, is nested in the centre of the stationary domain and rotates counter-clockwise. The inlet and outlet boundaries are indicated, in addition to the location of the free surface. The sides and bottom surfaces are free-slip walls and the top surface is a zero-relative-static-pressure-gradient opening

8 m diameter is nested in the centre of the larger stationary domain. A rectangular blade with the same surface area and curvature as a standard hatchet blade is located in the rotating domain at a radial distance of 2.4 m from the centre, with its top edge flush with the surface of the water at the beginning of the drive. This radial position of the blade represents the outboard length of the oar (the distance from the oarlock to the tip of the blade). The interface between the outer stationary domain and the inner rotating domain allows fluid to cross seamlessly. A rigid mesh within the rotating domain allows oar rotation by rotating the entire cylindrical domain itself. The shell velocity is simulated by the bulk velocity of the fluid flowing through the domain. An inlet boundary condition is located at the bow end of the domain, with the fluid velocity specified. The parallel surface, at the stern end of the domain, is a zero-relative-static-pressure outlet boundary. The two perpendicular sides of the domain as well as the bottom surface are modelled as free-slip walls. Domain size independence testing indicated that the locations of these walls are sufficiently far from the deviations of the mean flow caused by the blade, and so modelling them as free slip is reasonable. The top surface is a zero-relative-static-pressure opening with no velocity gradient perpendicular to the boundary.

2.2 Rowing stroke model

The rowing stroke model is based on force balances on the shell and the rowers. By specifying an angular velocity of the oar and the motion of the crew within the shell, the shell velocity is calculated using the propulsive force generated by the blade in the water, an analytical treatment of the drag on the shell, and the momentum of the rowers. The force balance is stated as

$$\boldsymbol{F}_{\text{net,shell}} = \boldsymbol{F}_{\text{propulsive,crew}} + \boldsymbol{F}_{\text{momentum,crew}} + \boldsymbol{F}_{\text{drag,shell}} \tag{1}$$

where

$$\boldsymbol{F}_{\text{propulsive,crew}} = n\boldsymbol{F}_{\text{propulsive}} \tag{2}$$

$$\boldsymbol{F}_{\text{momentum,crew}} = m_{\text{crew}}\boldsymbol{a}_{\text{relative,crew}} \tag{3}$$

$$\boldsymbol{F}_{\text{drag,shell}} = k\boldsymbol{v}_{\text{shell}}^2 \tag{4}$$

In equation (2), the propulsive force $\boldsymbol{F}_{\text{propulsive,crew}}$ is the force of the water acting on a single blade in the direction of the shell motion, $\boldsymbol{F}_{\text{propulsive}}$, multiplied by n, the number of oars. $\boldsymbol{F}_{\text{momentum,crew}}$ is due to the relative motion of the crew within the shell. It is assumed that each rower is a point mass located at their centre of mass and are all perfectly synchronized with one another. The effect of rower momentum is determined using equation (3) which is calculated from the mass m_{crew} of the crew and their instantaneous acceleration $\boldsymbol{a}_{\text{relative,crew}}$ relative to the shell centre line, which is based on $\boldsymbol{v}_{\text{relative,crew}}$ (Fig. 4). This relative motion of the crew, obtained from data from W. C. Atkinson (2009, personal communication), was derived from estimates of the position of components of the rower's body throughout the stroke in relation to the known oar angular position. The hydrodynamic drag force $\boldsymbol{F}_{\text{drag,shell}}$ experienced by the shell can be subdivided into skin friction drag, form drag, and wave drag. Experiments carried out [**5**] indicated that skin friction accounts for roughly 93 per cent of the hydrodynamic drag and is highly dependent on the shell velocity. In equation (4), the drag force acting on the shell is a function of the square of the instantaneous shell velocity $\boldsymbol{v}_{\text{shell}}$ and a constant drag factor k where

$$k = 1.07 \times \frac{1}{2} c\rho A_{\text{shell}} = 6.0\,\text{N s}^2/\text{m}^2 \tag{5}$$

In equation (5), the water density ρ $(=997\,\text{kg/m}^3)$ and the wetted surface area A_{shell} of the shell (i.e. the area of the hull that is in contact with the water) are known. The wetted shell area is assumed to be constant throughout the stroke. Although fluctuations in the actual wetted area caused by pitch and heave of the shell exist owing to the motion of the crew's centre of mass, these variations are not large and do not strongly impact on the magnitude of the shell drag force. A constant non-dimensional skin friction drag coefficient $(c = 0.002\,25)$ was calculated using the ITTC 1957 Hull Friction Resistance Correlation Line. This value is close to an experimental coefficient of 0.002 24 determined experimentally [**5**] for an eight-oared shell. A study by McMahon [**12**] declared that the values of this coefficient are similar for all racing shells, independent of their size. The factor of 1.07 is included, as recommended by Wellicome [**5**], to account for the form drag and wave drag.

Using the instantaneous net force $\boldsymbol{F}_{\text{net,shell}}$ on the shell and the combined mass m_{total} of the crew and shell, the shell acceleration is calculated as

$$\boldsymbol{a}_{\text{shell}} = \frac{\boldsymbol{F}_{\text{net,shell}}}{m_{\text{total}}} \tag{6}$$

The flow velocity is updated at each time step Δt based on the shell velocity $\boldsymbol{v}_{\text{shell},t-1}$ at the previous time step and $\boldsymbol{a}_{\text{shell}}$ using the relation

$$\boldsymbol{v}_{\text{shell},t} = \boldsymbol{v}_{\text{shell},t-1} + \boldsymbol{a}_{\text{shell}}\,\Delta t \tag{7}$$

To simulate the motion of the shell at the catch, the bulk flow within the domain is initialized to match the shell velocity immediately at the beginning of the drive. A smooth blade entry at the catch is similarly modelled by initializing the angular velocity of the

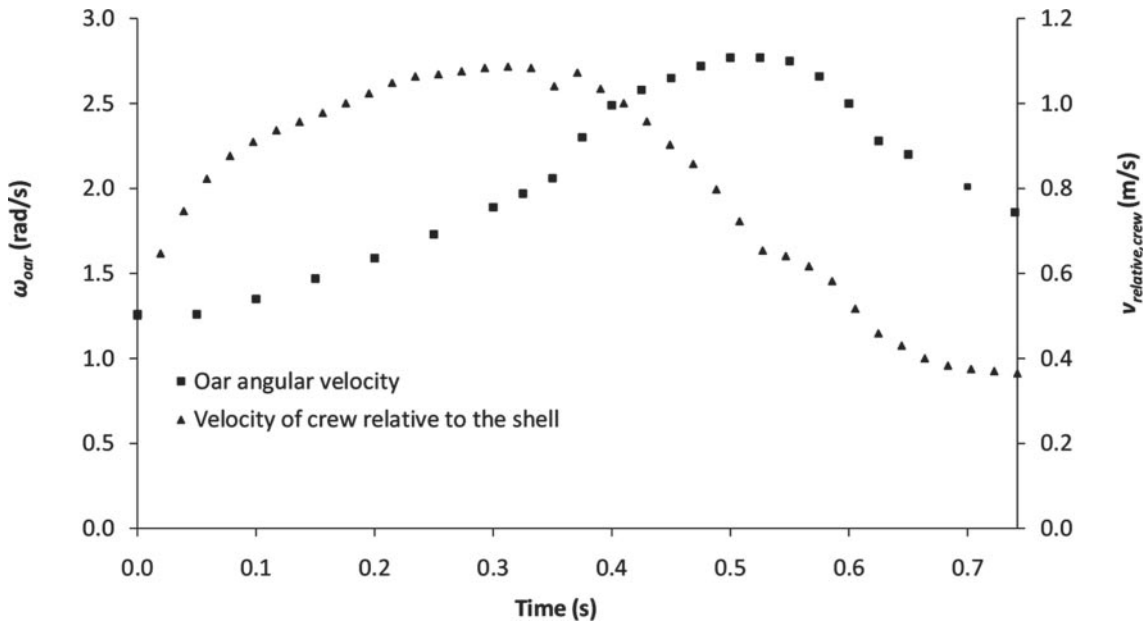

Fig. 4 Oar angular velocity during the drive (indicated by full squares) and velocity of the crew relative to the shell (indicated by full triangles) obtained from V. Kleshnev and W. C. Atkinson (2009, personal communication)

Table 1 Parameters of the rowing stroke (obtained from V. Kleshnev, 2009, personal communication)

Boat class	Heavy Men 4
Mass m_{crew} of the crew	376 kg
Mass m_{shell} of the shell	50 kg
Shell wetted area A_{shell}	5 m^2
Oar outboard length	2.4 m
Stroke rate	31.1 strokes/min
Stroke period	1.93 s
Drive period	0.74 s

rotating domain to match the oar angular velocity at the beginning of the drive.

2.3 Modelled stroke quantities

To provide a basis for comparison of the results, the physical parameters of the rowing stroke were set to match those used in Kleshnev's experiments involving a shell which has four sweep rowers (each holding one oar) and which is being rowed in actual conditions (Table 1). In his experiments, Kleshnev instrumented rowing equipment to obtain data relating the linear velocity of the shell to the oar angular velocity during a stroke. Details of these measurement techniques are available [**1**]. The oar angular velocity $\boldsymbol{\omega}_{\text{oar}}$ (Fig. 4), specified as an input in the present simulation, is based on experimental data from V. Kleshnev (2009, personal communication).

2.4 Numerics

The free-surface distinction between the water and air phases is accomplished using a volume-of-fluid (VOF) multi-phase method [**13**]. All fluid phases within the domain are treated as a single continuum flow field, sharing common transported velocity and pressure quantities. The volume fraction φ of each fluid within each domain element is tracked during the solution stage. Most elements contain either entirely water ($\varphi_{\text{water}} = 1$) or entirely air ($\varphi_{\text{air}} = 1$). Elements along the interface between the water and air take on a fractional φ value ($0 < \varphi < 1$). At a given instance, the location of the free surface can be defined by combining elements of fractional φ [**14**]. The validity of a homogeneous multi-phase flow treatment when applied to free-surface waves is provided by a study performed by Zwart *et al.* [**15**]. Using the homogeneous multi-phase flow model provided in ANSYS CFX, they were able to simulate the wave pattern generated by a moving ship hull that agreed very well with experimental data. The ability of this multi-phase model to simulate surface waves accurately provides confidence for its use when modelling the free-surface deformation around a rowing blade in motion.

The flow is solved using the three-dimensional unsteady turbulent Navier–Stokes equations, modified to account for multi-phase flow. The transport equations are similar to those for single-phase flow but incorporate the individual density and viscosity of each fluid phase. Assuming that there is volume conservation within each domain element

$$\varphi_{\text{water}} + \varphi_{\text{air}} \equiv 1 \tag{8}$$

and that transported velocity and pressure quantities are the same across each fluid phase, the conservation-of-mass equations for the water and air phases are

$$\frac{\partial}{\partial t}(\varphi_{\text{water}}\rho_{\text{water}}) + \frac{\partial}{\partial x_i}(\varphi_{\text{water}}\rho_{\text{water}}u_i) = 0 \tag{9}$$

$$\frac{\partial}{\partial t}(\varphi_{\text{air}}\rho_{\text{air}}) + \frac{\partial}{\partial x_i}(\varphi_{\text{air}}\rho_{\text{air}}u_i) = 0 \tag{10}$$

respectively. The conservation-of-momentum equations are defined as

$$\frac{\partial}{\partial t}(\rho u_j) + u_i\frac{\partial}{\partial x_i}(\rho u_j) = -\frac{\partial p}{\partial x_j} + (\mu + \mu_{\text{t}})\frac{\partial^2 u_j}{\partial x_i^2} + \boldsymbol{S} \tag{11}$$

where μ_{t} is the turbulence viscosity. Here, the density ρ and dynamic viscosity μ are volume averages of the properties of each of the fluid phases, given by

$$\rho = \varphi_{\text{water}}\rho_{\text{water}} + \varphi_{\text{air}}\rho_{\text{air}} \tag{12}$$

$$\mu = \varphi_{\text{water}}\mu_{\text{water}} + \varphi_{\text{air}}\mu_{\text{air}} \tag{13}$$

and S denotes additional momentum source terms applied to the flow in the domain. $\boldsymbol{S}_{\text{shell}}$ is included in the streamwise (x component of the) momentum equation to simulate a uniform shell velocity throughout the domain, according to

$$\boldsymbol{S}_{\text{shell}} = \rho\boldsymbol{a}_{\text{shell}} \tag{14}$$

There are three additional source terms included in the streamwise and spanwise (x and y components respectively) momentum equations for the flow within the rotating domain. These terms account for the effect of the Coriolis force, the centrifugal force, and a Euler force associated with the non-uniform angular acceleration of the domain, according to

$$\boldsymbol{S}_{\text{Coriolis}} = -2\rho\boldsymbol{\omega}_{\text{oar}}\boldsymbol{v}_{\text{shell}} \tag{15}$$

$$\boldsymbol{S}_{\text{centrifugal}} = -\rho\boldsymbol{\omega}_{\text{oar}} \times (\boldsymbol{\omega}_{\text{oar}}r) \tag{16}$$

$$\boldsymbol{S}_{\text{Euler}} = -\rho\frac{\partial\boldsymbol{\omega}_{\text{oar}}}{\partial t}r \tag{17}$$

where r is the radial location from the axis of rotation.

To allow fluid to pass seamlessly across the sliding interface between the outer stationary domain and inner rotating domain, which have dissimilar meshes on either side, an interface connection model is required. At the start of each time step, this model determines the relative position of each side of the sliding interface, and the surface flux of the mass and momentum quantities on either side of the interface is discretized. In order to match the fluxes across the interface surface, balance equations are generated on the basis of the flux contributions from either side. These balance equations are then applied along the interface region, ensuring a flow balance across the surface.

Turbulence is modelled using a shear stress transport (SST) model [**16**]. The SST turbulence model was selected for its ability to model accurately the flow separation from a foil in an adverse pressure gradient [**17**]. This model combines the k–ε turbulence model [**18**] and the k–$\boldsymbol{\omega}$ turbulence model [**19**] by transitioning from the k–ε model in free-shear-flow regions to the k–$\boldsymbol{\omega}$ model in near-wall regions using a blending function. Transport of principal turbulent shear stresses, which are important in the prediction of adverse pressure gradients, are also included in the eddy viscosity formulation of the SST model. The turbulence intensity at the inlet, defined as the ratio of the turbulent velocity fluctuations to the mean fluid velocity ($I = u'/U$), is set at 5 per cent, and the turbulence length scale is equal to the depth of the water (1.5 m).

An unstructured tetrahedral domain mesh was generated using ANSYS CFX-Mesh. A maximum element edge length of 10 cm is used in the bulk flow region. A smaller maximum edge length of 0.5 cm is used near the blade, and a set of boundary layer cells 3 mm thick and 25 layers deep is applied at the blade surface to resolve the flow detail there. Grid testing revealed that a 2.8×10^6 element mesh yields grid-independent results, having less than a 1 per cent difference in the calculated shell velocity at each time step compared with a 1.4×10^6 element mesh. Time-step testing indicated that a 0.005 s interval resolves the time dependences of the flow, with less than a 1 per cent difference in the calculated shell velocity at each time step when compared with a 0.01 s step size.

The conservation-of-mass and conservation-of-momentum equations are solved using a high-resolution advection scheme, while the turbulence quantities are solved using an upwind scheme. A second-order backward Euler transient scheme is used for the conservation equations, and a first-order backward Euler transient scheme for the turbulence quantities. To maintain a distinct boundary between the air and water phases, the compressive advection discretization scheme for the volume fraction terms allows the high-resolution blending function to be greater than 1. This gives rise to antidiffusive behaviour, allowing the scheme to operate with a relatively large time step and still to maintain the required compressiveness at the free surface to provide a sharp interface [**15**]. Using the ANSYS CFX commercial CFD code, the governing equations are solved at each time step until the r.m.s. residuals of the conservation-of-mass and conservation-of-momentum equations fall below 10^{-4}.

3 RESULTS AND DISCUSSION

3.1 Model validation

The primary source of validation for the model lies in its ability to predict the shell velocity during a stroke. Figure 5 plots the shell velocity during both the drive and the recovery phases for the simulation together with experimental values obtained by V. Kleshnev (2009, personal communication). The recovery phase of the stroke is modelled identically with the drive phase, except for the absence of the propulsive force term, according to

$$\boldsymbol{F}_{\text{net,shell}} = \boldsymbol{F}_{\text{momentum,crew}} + \boldsymbol{F}_{\text{drag,shell}} \tag{18}$$

The shell velocity at the end of the stroke cycle (and thus immediately before the next cycle begins) is within 1 per cent of the initial shell velocity, which is expected. The simulated shell velocity through the stroke follows the same shape as observed in the experiment, although the average shell velocity from the simulation is 4.1 per cent lower than the experimental value. The simulation is sensitive to the input of an oar angular velocity which is based on experimentally obtained data [**1**], and a relative crew velocity which is modelled in part from the oar angular position. Any errors in these temporal input values will have an impact on the simulated results. In addition, as described earlier, the shape of the blade in the simulation is a curved rectangle with the same surface area as a hatchet blade. Although this geometry is not the same as was used in the experiments, it represents a good approximation to an actual rowing blade, for which dimensional data were unavailable. This geometry has also been used in previous studies investigating drag and lift effects for stationary and moving blades [**7, 9, 11**]. That the model is able to simulate the shape of the experimental shell velocity profile gives confidence that it is able to both replicate the physics of the rowing stroke and capture the hydrodynamic characteristics of a blade in motion.

Observing the motion of the centre of the blade chord through the water from a stationary reference frame, it follows a *figure-nine* pattern (Fig. 6) similar to what has been observed experimentally (Fig. 2).

From the calculated flow and pressure fields around the blade throughout the drive, the resultant force on the blade can be determined. This force can be decomposed in a number of ways. Figure 7 plots the blade force component in the direction of the shell motion (the propulsive force, $\boldsymbol{F}_{\text{propulsive}}$). Also plotted are the blade drag and lift forces.

3.2 Flow phases during the rowing stroke

Based on the relative blade motion in the water and the temporal development of the instantaneous blade forces, it is observed that there are six distinct flow regimes encountered during the drive. These flow phases are outlined in Table 2. A detailed examination of the flow throughout the stroke gives insight as to the mechanisms defining each phase.

3.2.1 *Phase I*

From blade entry in the water at the catch ($t = 0$ s) until 0.35 s, phase I accounts for nearly half of the drive time. Immediately after entering the water at the beginning of the drive, the blade moves both

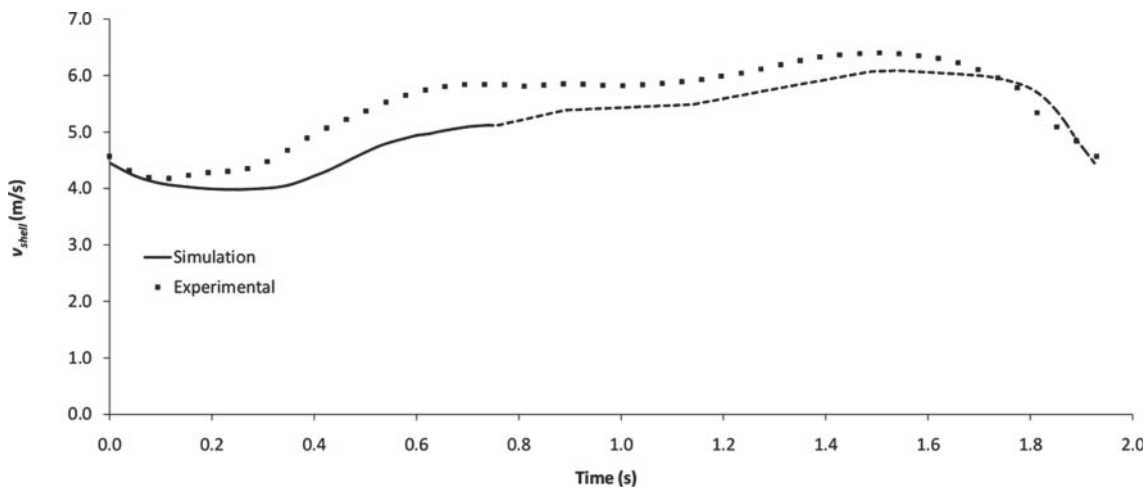

Fig. 5 Comparison of simulated and experimental shell velocities during the stroke. The simulation data are indicated for the drive by a solid curve, and for the recovery by a dashed curve. The experimental data are from V. Kleshnev (2009, personal communication) and are indicated by full squares

laterally away from the shell and with a positive slip (Fig. 6). The blade experiences a shallow but gradually increasing $\alpha_{nominal}$ during this phase, rising from 0° to 25° (Fig. 8(a)). As $\alpha_{nominal}$ increases, there is an increasing pressure difference across the blade (up to about 1.5 kPa) located near the tip, which is mostly due to the increasing horizontal flow velocity over the back surface of the blade (Fig. 8(b)). Initially, the flow is almost entirely horizontal along the blade, moving from the tip edge towards the shaft. As $\alpha_{nominal}$ increases, flow begins to spill over the top and bottom edges of the blade, and small horizontal vortices with their cores aligned parallel to the top and bottom edges of the blade are formed on the back surface (Fig. 8(c)). These vortices aid in keeping the flow attached to the back of the blade throughout this phase, even when the angle of attack at the blade tip is approximately 25°, which in turn keeps drag minimal. The flow over the top edge of the blade also leads to a growing surface deformation (Fig. 8(d)). Towards the end of this phase, a small flow separation near the blade tip occurs, caused by the formation of a vertical vortex with its core aligned parallel to the tip edge (Fig. 8(c)). The resulting suction effect on the back of the blade leads to an increasing lift force. Correspondingly, the propulsive force in phase I is primarily due to lift on the blade (Fig. 7).

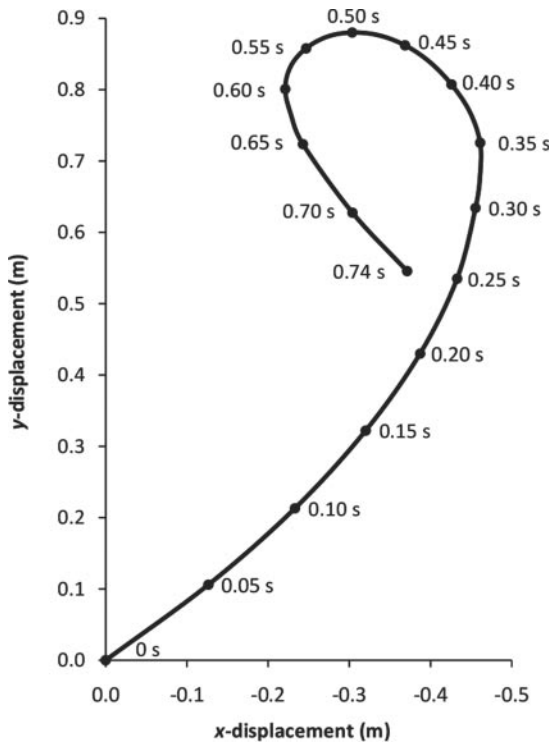

Fig. 6 From a stationary frame of reference for the present simulation, an overhead view indicating the calculated path of the centre of the blade chord line through the water during a stroke. The shell is moving from left to right

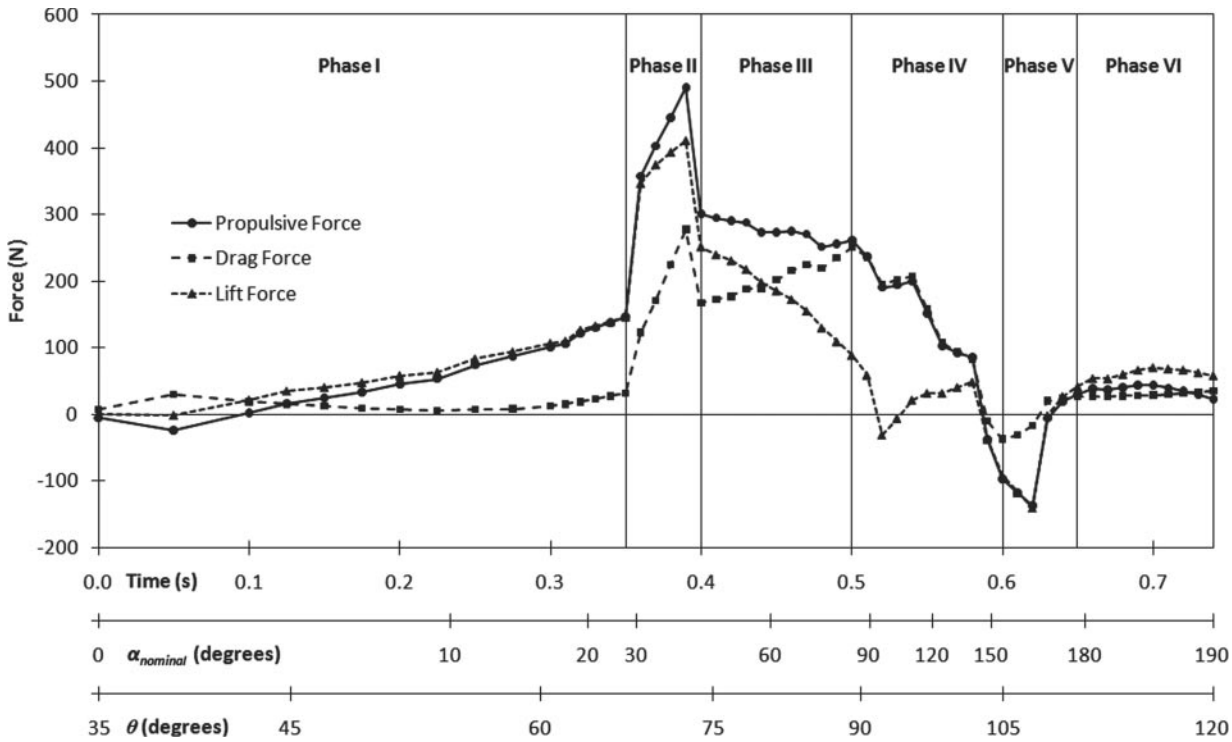

Fig. 7 Temporal development of forces on the blade during a stroke, divided into six phases. The propulsive force is indicated by a solid curve, the drag force by a dashed curve, and the lift force by a dotted curve. Additional abscissa axes include the nominal angle of attack on the blade and the bow angle of the oar

Table 2 Behaviour of the blade forces, as well as the nature of slip, in each phase of the drive

Phase	Time (s)	$F_{propulsive}$	F_{drag}	F_{lift}	Slip
I	0–0.35	Low	Very low	Low	Positive
II	0.35–0.4	Very high	Moderate	Very high	Negative
III	0.4–0.5	High	High	Moderate	Negative
IV	0.5–0.6	Moderate	Moderate	Low	Negative
V	0.6–0.65	Negative	Negative	Negative	Positive
VI	0.65–0.74	Very low	Very low	Very low	Positive

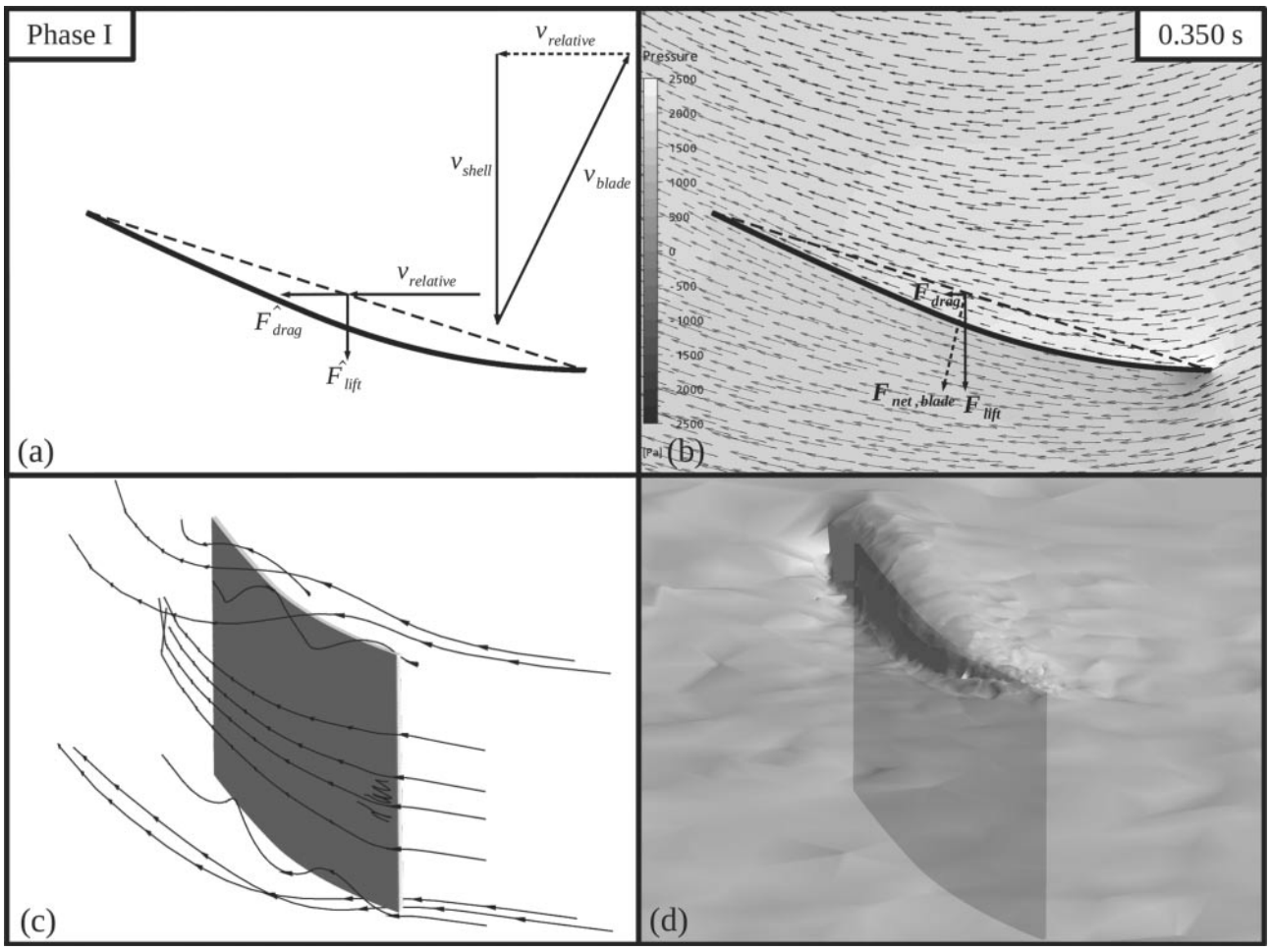

Fig. 8 Flow characteristics for phase I of the drive (at 0.35 s). (a) The shell is moving downwards and the oar is rotating with a counterclockwise angular velocity. The velocities and forces are as in Fig. 1. (b) Pressure contour and velocity vectors of the flow for a plane slice through the middle of the blade. The net force on the blade, decomposed into drag and lift components, is indicated. (c) Streamlines highlighting important flow characteristics. (d) Contour of the free surface in the region surrounding the blade

3.2.2 Phase II

From 0.35 s to 0.40 s the blade is still moving laterally away from the shell, but now with negative slip (Fig. 6). In this phase, $\alpha_{nominal}$ increases at a much quicker rate than in phase I, rising from 25° to 45° in 0.05 s (Fig. 9(a)). The flow increasingly spills over the top edge of the blade, resulting in a growing bulge in the free surface over, and depression behind, the blade (Figs 9(c) and (d)). Flow over the bottom edge also increases with increasing $\alpha_{nominal}$. At 0.36 s there is a sudden rise in the pressure difference across the blade (approximately 4 kPa), leading to a rapid increase in the propulsive force that is primarily lift induced (Fig. 9(b)). The drag and lift forces continue

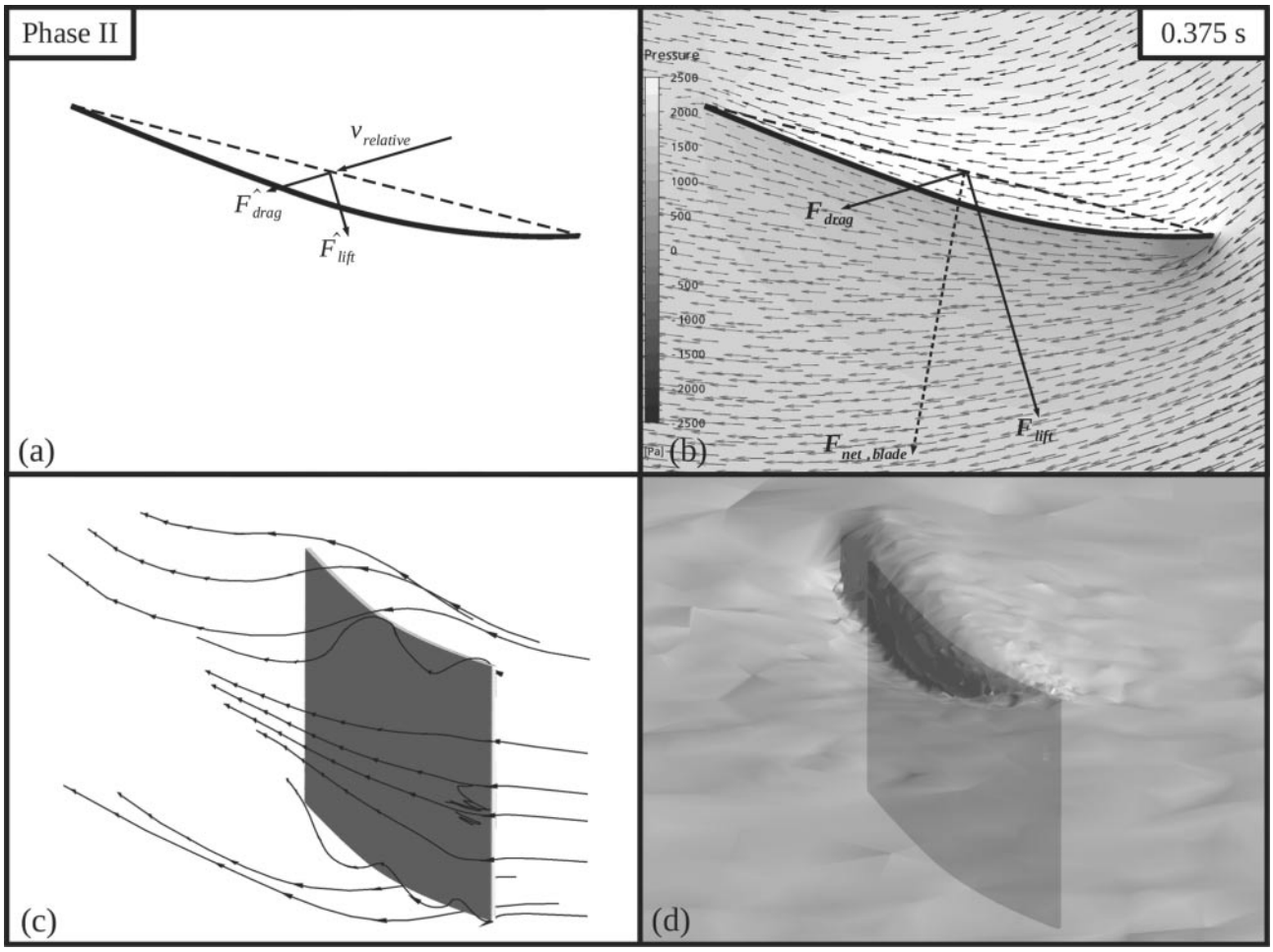

Fig. 9 Flow characteristics for phase II of the drive (at 0.375 s): (a)–(d) are as in Fig. 8

to increase until 0.39 s, at which point the propulsive force reaches its maximum value (Fig. 7). This is followed by a sharp drop in the propulsive force at 0.4 s, again largely caused by lift effects.

The lift behaviour in this phase may be attributed to dynamic stall characteristics of the blade. Experiments on pitching airfoils with a rapidly increasing angle of attack reveal a similar increase in lift, followed by a sharp decrease over a short period of time [**20**]. As the incident flow on a rapidly pitching airfoil increases beyond the angle of attack for static stall (the angle of attack for a stationary airfoil where the onset of flow separation past the leading edge occurs, leading to a large reduction in lift), a vortex develops at the leading edge. As this vortex grows and is convected downstream along the airfoil surface, its suction effect causes an increase in lift. When the vortex is eventually shed from the surface, the lift decreases sharply and the net force on the airfoil becomes primarily drag induced. This phenomenon is caused by a time lag in the pressure response to the changing angle of attack, causing the airfoil to experience a smaller angle of attack than it would under static conditions. Although these experiments were performed on high-aspect-ratio airfoils (primarily two-dimensional flow along the chord line), the effect that the formation and motion of vortices have on pressure changes for the low-aspect-ratio rowing blade can be drawn. The onset and growth of vortices, both horizontal and vertical, on the low-pressure (back) surface of the blade leads to a decreasing relative pressure there, resulting in a higher lift force. As vortices are shed, there is a rapid decrease in the relative pressure at the back of the blade, leading to an abrupt reduction in lift.

There is reason to believe, however, that the behaviour of the blade force in this phase may also be affected by inaccuracies in the input data. A sudden rise in the oar angular velocity at approximately 0.35 s (Fig. 4) may exacerbate the jump in blade force occurring at the same time. Nevertheless, the dynamic stall characteristics of the blade as outlined in this section are expected to hold true even in the absence of an abrupt rise in the oar angular velocity,

as dynamic stall behaviour is characterized by the steadily increasing angle of attack on the blade.

3.2.3 Phase III

From 0.4 s to 0.5 s, the blade continues to move laterally away from the shell, still with a negative slip (Fig. 6). The nominal angle of attack continues to sweep rapidly across the blade, increasing from 50° to 85° (Fig. 10(a)). The rising $\boldsymbol{\alpha}_{\text{nominal}}$ causes the vertical vortex near the blade tip to grow as the flow approaches the blade at a steeper incidence. By 0.45 s ($\boldsymbol{\alpha}_{\text{nominal}} \approx 60°$), flow reversal is seen on most of the back surface of the blade, explaining the decreasing lift force during this phase (Fig. 10(b)). Flow over the top and bottom edges of the blade also increases as $\boldsymbol{\alpha}_{\text{nominal}}$ approaches normal to the blade chord line, leading to growing horizontal vortices on the back of the blade (Fig. 10(c)). The strengthening horizontal vortices caused by flow spillover from the top and bottom edges maintain a high pressure difference across the blade (approximately 2.5 kPa), causing the free-surface bulge and depression to continue to grow (Fig.10(d)). These horizontal vortices, which are more pronounced towards the shaft side of the blade, and the persistence of the vertical vortex near the tip, explain the rise in drag force during this phase. This increasing influence of drag during this phase helps maintain a high blade propulsive force (Fig. 7).

3.2.4 Phase IV

After 0.50 s, the blade begins to move laterally back towards the shell, still with negative slip (Fig. 6). The nominal angle of attack moves past, perpendicular to the blade surface, making the shaft side the leading edge (Fig. 11(a)). The nominal angle of attack increases at its quickest rate, reaching 155° (25° as seen by the shaft side) by 0.60 s. With the aid of the persisting vertical vortex near the blade tip, the flow once again attaches to the back of the blade (Fig. 11(b)). The strength of this vertical vortex causes the flow behind the blade to converge near the tip, where it meets the flow moving past the trailing edge from the front of the blade. The reattachment of the flow and the

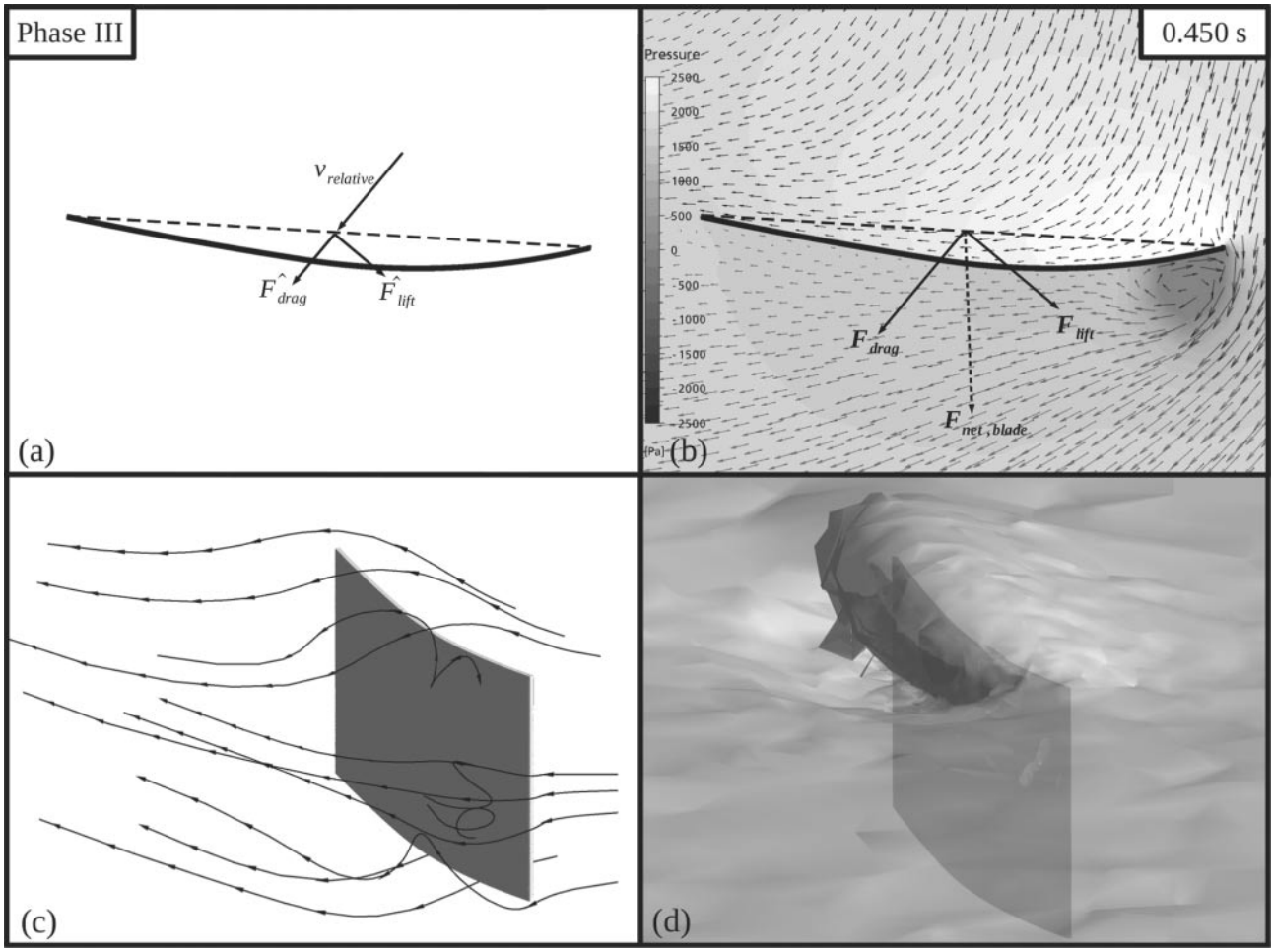

Fig. 10 Flow characteristics for phase III of the drive (at 0.45 s): (a)–(d) are as in Fig. 8

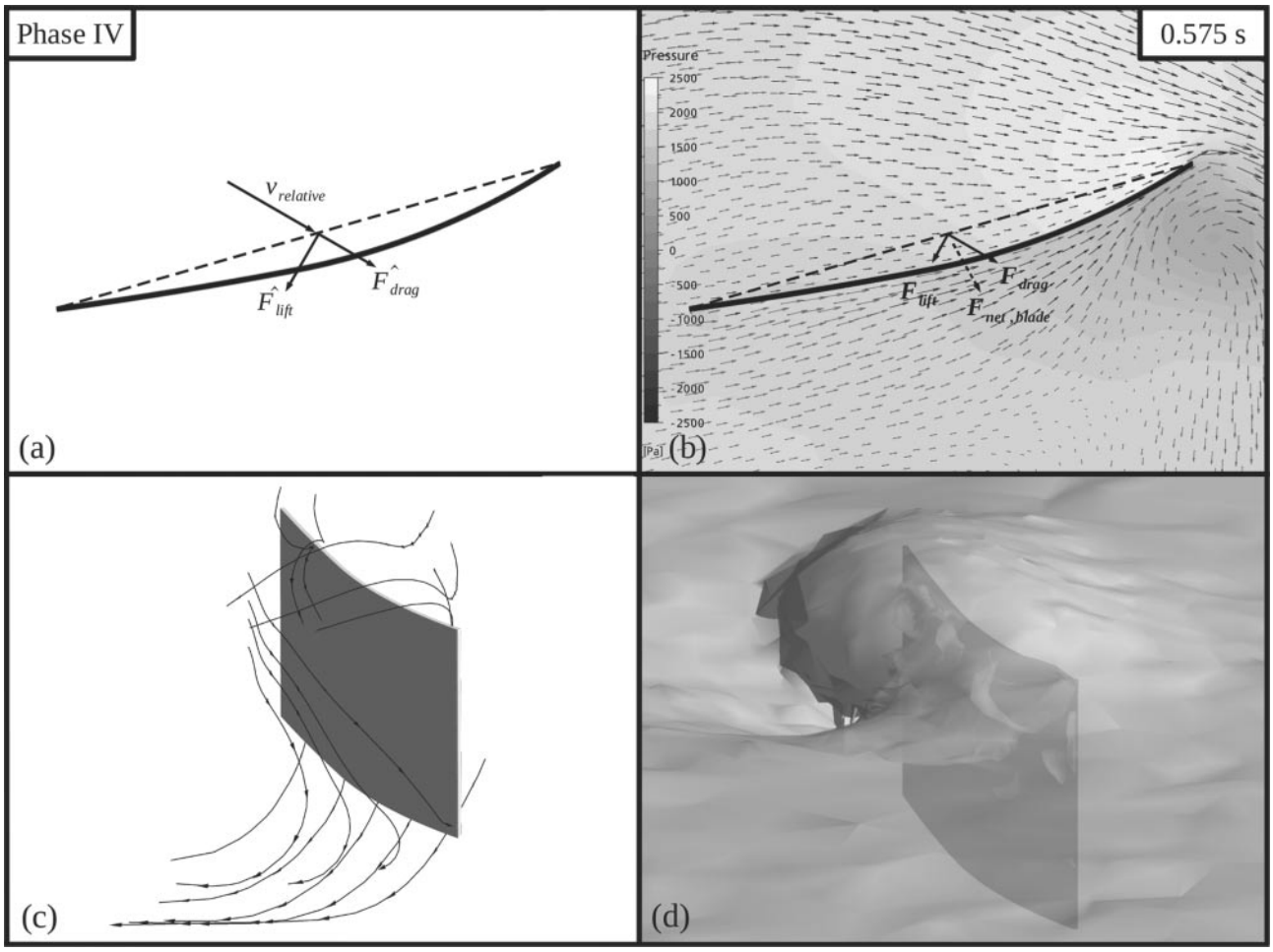

Fig. 11 Flow characteristics for phase IV of the drive (at 0.575 s): (a)–(d) are as in Fig. 8

presence of the vertical vortex near the tip help to maintain a strong pressure difference across the blade (approximately 2.5 kPa), leading to a slight rise in the lift force and a drop in the drag at 0.55 s. Flow over the top and bottom edges continues to increase during this phase, causing the horizontal vortices located at the top and bottom of the back surface to grow (Fig. 11(c)). With the flow now approaching the blade from the shaft side, it stretches these vortices from the shaft side of the blade towards the tip. This is reflected in the free-surface bulge and depression also moving towards the tip (Fig. 11(d)). At 0.575 s, the vertical vortex at the tip sheds from the blade as the flow over the back surface of the blade increases. The shedding of this vortex explains the drop in pressure difference across the surface (down to about 1 kPa), which leads to a sharp decrease in $\boldsymbol{F}_{\text{propulsive}}$ by the end of this phase (Fig. 7).

3.2.5 *Phase V*

Between 0.6 s and 0.65 s the blade continues to move laterally towards the shell, and the slip becomes positive again (Fig. 6). The nominal angle of attack continues to increase, reaching 180° by the end of the phase (Fig. 12(a)). The large horizontal vortex at the bottom of the blade detaches in this phase, causing the flow to converge further on the back surface of the blade near the tip, which results in a high-pressure region (about 2 kPa) that now occurs on the back of the blade near the shaft (Fig. 12(b)). This leads to a switch in the direction of the pressure difference across the blade, causing negative drag and lift for 0.05 s of this phase. The horizontal vortices caused by increasing flow over the top and bottom edges continue to strengthen as the flow approaches from an increasingly shallow $\boldsymbol{\alpha}_{\text{nominal}}$ (seen from the shaft side of the blade). These vortices drag the horizontal streamlines vertically on the back of the blade as the flow moves towards the tip (Fig. 12(c)). This is accompanied by the fact that the surface bulge and depression continue to move towards the tip (Fig. 12(d)). As the flow remains attached to the back of the blade, drag effects are minimal, and lift contributes primarily to the propulsive force. The reversed pressure difference in this phase causes the

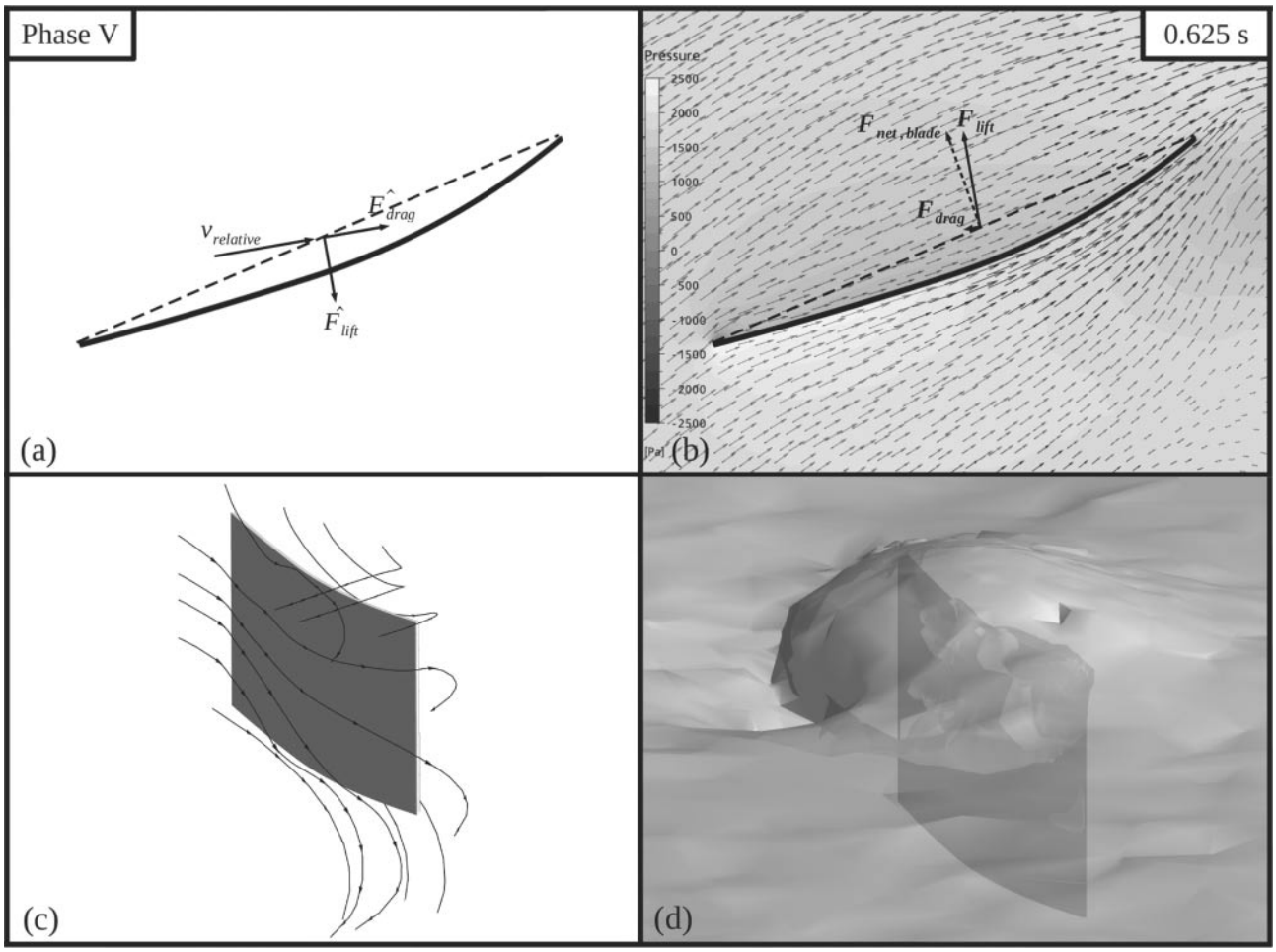

Fig. 12 Flow characteristics for phase V of the drive (at 0.625 s): (a)–(d) are as in Fig. 8

propulsive force vector to be directed opposite to the shell motion, acting to reduce the shell velocity (Fig. 7). Similar to the sudden rise in the oar angular velocity in phase II, which may have exaggerated the blade force values, a relatively abrupt decrease in the oar angular velocity at approximately 0.6 s (Fig. 4) may also explain the negative blade force caused by the occurrence of the high-pressure region behind the blade as the flow reacts to the decreasing blade velocity. Although the negative blade propulsive force may be inaccurate, a decreasing force at this point in the stroke is still expected on the basis of the increasingly shallow angle of attack and lower oar angular velocity.

3.2.6 Phase VI

During the final phase of the drive (from 0.65 s to 0.74 s), the blade continues to move laterally towards the shell with a positive slip (Fig. 6). The nominal angle of attack is still increasing, but at a much lower rate, reaching 190° by the end of the drive, with the flow becoming incident on the back surface of the blade (Fig. 13(a)). The flow remains attached on both sides of the blade, and the horizontal vortex near the top edge persists and continues to grow (Fig. 13(c)), leading to a low-relative-pressure region (about 2 kPa) at the back surface of the blade near the tip (Fig. 13(b)). Although $\boldsymbol{\alpha}_{\text{nominal}}$ is incident on the back surface of the blade, the low-pressure region on this side causes a high flow velocity across this surface. This shallow $\boldsymbol{\alpha}_{\text{nominal}}$ causes the horizontal vortex present off the back of the blade near the bottom edge to continue to move radially outward towards the tip and beyond. Correspondingly, the blade slides away from the created bulge and depression, and these surface conditions begin to dissipate (Fig. 13(d)). Drag and lift are once again positive, acting in the direction of the shell and aiding propulsion. Drag is low in this phase, similar to phase I, owing to the shallow nominal angle of attack. The effect on the propulsive force is that it is low, but once again positive (Fig. 7).

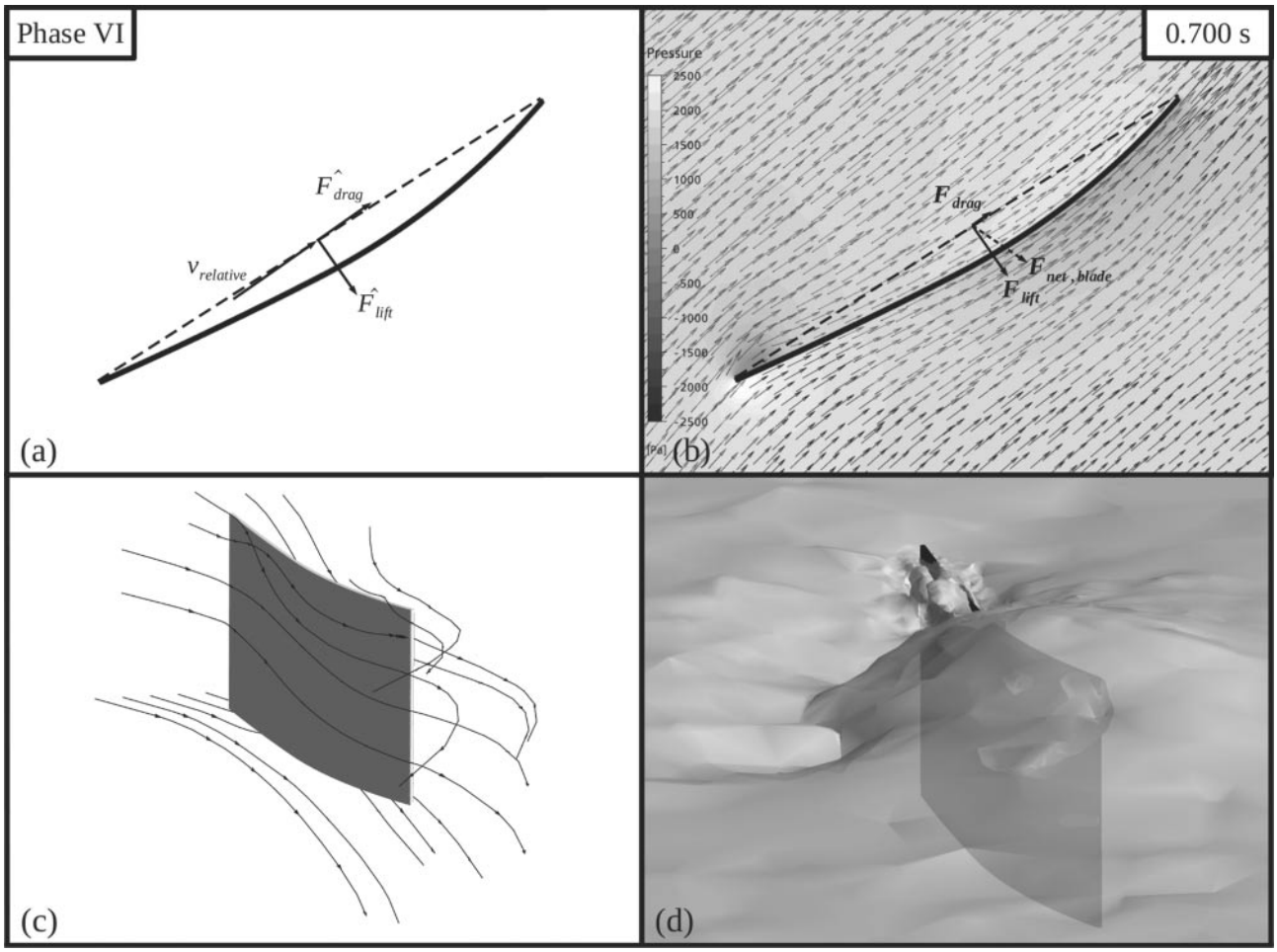

Fig. 13 Flow characteristics for phase VI of the drive (at 0.7 s): (a)–(d) are as in Fig. 8

4 CONCLUSIONS

An examination of the flow about a rowing blade during the stroke has shown that it exhibits significant transient behaviour. The flow can be divided into distinct characteristic phases based on the motion of the blade in the water and the relative blade forces. During the first half of the stroke the flow remains attached to the blade, which acts as a hydrofoil, generating primarily lift forces as the propulsive force increases. As the angle of attack increases further, dynamic stall characteristics of the blade explain a rise in lift beyond what would be expected under steady conditions, in turn increasing the propulsive force. The middle portion of the stroke maintains a high blade propulsive force that is heavily drag induced as the flow separates past the blade. The end of the stroke is characterized by a low propulsive force that is once again primarily lift induced, owing to the reattached flow at a shallow angle of attack. As mentioned earlier, the present model is sensitive to the input of oar angular velocity and relative crew velocity, and inaccuracies in the data used may lead to exaggerated blade forces (i.e. phases II and V). In spite of these potential inaccuracies, the gross features of the blade–water interaction throughout the stroke, outlined in the preceding paragraph, hold true. Rather than these results being taken as a definite depiction of the flow around a rowing oar blade, they should be interpreted as a general outline of the hydrodynamic behaviour of a blade during a stroke. An understanding of this transient flow behaviour about a rowing blade in motion will be of interest to several groups. Biomechanics researchers and coaches can use this information to optimize stroke mechanics, improving the rower's efficiency in transferring power into shell propulsion. Rowing oar designers can employ an advanced understanding of blade flow to create blade shapes which maximize the transfer of power input from the rower through the stroke into shell propulsion. Changes in blade shape ultimately leading to faster crews cannot, however, occur in isolation. An improved blade design must also be congruent with existing rowing technique, such that rowers can easily adapt to its introduction. Likewise, changes in the rowing stroke must also be acceptable, given the rowing blade being used. The collaboration

between those designing rowing blades and those using them, then, will certainly result in faster crews.

© Authors 2010

REFERENCES

1 **Kleshnev, V.** Propulsive efficiency of rowing. In Proceedings of the XVII International Symposium on *Biomechanics in sports*, Perth, Western Australia, Australia, 30 June–6 July 1999, pp. 224–228 (International Society of Biomechanics in Sports, Perth).

2 **Millward, A.** A study of the forces exerted by an oarsman and the effect on boat speed. *J. Sports Sci.*, 1987, **5**, 93–103.

3 **Brearley, M. N., de Mestre, N. J.,** and **Watson, D. R.** Modelling the rowing stroke in racing shells. *Mathl Gaz.*, 1998, **82**, 389–404.

4 **Pope, D. L.** On the dynamics of men and boats and oars. In *Mechanics and sport*, 1973, pp. 113–130 (ASME International, New York).

5 **Wellicome, J. F.** Some hydrodynamic aspects of rowing. In *Rowing – a scientific approach*, 1967, pp. 22–63 (A. S. Barnes & Co., Cranbury, New Jersey).

6 **Nolte, V.** Do you need hatchets to chop your water? *Am. Rowing*, 1993, **25**(4), 23–26.

7 **Caplan, N.** and **Gardner, T. N.** A mathematical model of the oar blade–water interaction in rowing. *J. Sports Sci.*, 2007, **25**, 1025–1034.

8 **Atkinson, W. C.** Validating the ROWING model, 2001, available from http://www.atkinsopht.com/row/validate.htm (access date 19 November 2008).

9 **Caplan, N.** and **Gardner, T. N.** Optimization of oar blade design for improved performance in rowing. *J. Sports Sci.*, 2007, **25**, 1471–1478.

10 **Macrosan, M. N.** The direction of water force on a rowing blade and its effect on efficiency. Mechanical Engineering Report 2008/03, University of Queensland, Brisbane, Queensland, Australia, 2008.

11 **Sliasas, A.** and **Tullis, S.** Numerical modelling of rowing blade hydrodynamics. *J. Sports Eng.*, 2009, **12**(1), 31–40.

12 **McMahon, T. A.** Rowing: a similarity analysis. *Science*, 1971, **173**, 349–351.

13 **Hirt, C. W.** and **Nichols, B. D.** Volume of fluid (VOF) method for the dynamics of free surface boundaries. *J. Comput. Phys.*, 1981, **39**, 201–225.

14 **Gueyffier, D., Li, J., Nadim, A., Scardovelli, R.,** and **Zaleski, S.** Volume-of-fluid interface tracking with smoothed surface stress methods for three-dimensional flows. *J. Comput. Phys.*, 1999, **152**, 423–456.

15 **Zwart, P. J., Godin, P. G., Penrose, J.,** and **Rhee, S. H.** Simulation of unsteady free-surface flow around a ship hull using a fully coupled multi-phase flow method. *J. Mar. Sci. Technol.*, 2008, **13**, 346–355.

16 **Menter, F. R.** Two-equation eddy–viscosity turbulence models for engineering applications. *AIAA J.*, 1994, **32**(8), 1598–1605.

17 **Menter, F. R., Kuntz, M.,** and **Langtry, R.** Ten years of industrial experience with the SST turbulence model. In *Turbulence, heat and mass transfer 4*, 2003, pp. 625–632 (Begell House, New York).

18 **Jones, W. P.** and **Launder, B. E.** The prediction of laminarization with a two-equation model of turbulence. *Int. J. Heat Mass Transfer*, 1972, **15**(2), 301–314.

19 **Wilcox, D. C.** Reassessment of the scale-determining equation for advanced turbulence models. *AIAA J.*, 1988, **26**(11), 1299–1310.

20 **Carr, L. W.** Progress in analysis and prediction of dynamic stall. *J. Aircr.*, 1988, **25**, 6–17.

APPENDIX

Notation

$\boldsymbol{a}_{\text{relative,crew}}$	acceleration of the crew relative to the shell
$\boldsymbol{a}_{\text{shell}}$	acceleration of the shell
A_{shell}	wetted surface area of the shell
c	non-dimensional shell skin friction drag coefficient
$\boldsymbol{F}_{\text{drag}}$	drag force on the blade
$\boldsymbol{F}_{\text{drag,shell}}$	drag force on the shell
$\boldsymbol{F}_{\text{lift}}$	lift force on the blade
$\boldsymbol{F}_{\text{momentum,crew}}$	momentum force created by the relative motion of the crew
$\boldsymbol{F}_{\text{net,blade}}$	net force on the blade
$\boldsymbol{F}_{\text{net,shell}}$	net force on the shell
$\boldsymbol{F}_{\text{propulsive}}$	propulsive force on the blade
$\boldsymbol{F}_{\text{propulsive,crew}}$	combined propulsive blade forces of the crew
I	turbulence intensity
k	drag factor
m_{crew}	mass of the crew
m_{total}	mass of the crew and shell
n	number of oars
p	mean pressure
r	radial location from the axis of rotation
$\boldsymbol{S}_{\text{centrifugal}}$	source term for the centrifugal force
$\boldsymbol{S}_{\text{Coriolis}}$	source term for the Coriolis force
$\boldsymbol{S}_{\text{Euler}}$	source term for the Euler force
$\boldsymbol{S}_{\text{shell}}$	source term for the shell velocity
t	time
u'	fluctuating velocity component
u_i	velocity component
U	mean velocity component
$\boldsymbol{v}_{\text{blade}}$	linear velocity of the blade
$\boldsymbol{v}_{\text{relative}}$	flow velocity incident on the blade
$\boldsymbol{v}_{\text{relative,crew}}$	velocity of the crew relative to the shell
$\boldsymbol{v}_{\text{shell}}$	velocity of the shell
x_i	Cartesian coordinate
$\boldsymbol{\alpha}_{\text{nominal}}$	nominal angle of attack of the flow on the blade
$\boldsymbol{\theta}_{\text{oar}}$	angular position of the oar
μ	dynamic viscosity
μ_{t}	turbulence viscosity
ρ	density
φ	volume fraction of fluid
$\boldsymbol{\omega}_{\text{oar}}$	angular velocity of the oar